Journal of Energy Storage 134 (2025) 118134

Contents lists available at ScienceDirect

Journal of Energy Storage

journal homepage: www.elsevier.com/locate/est

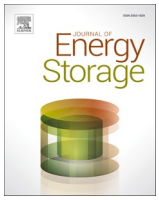

Research papers

Computationally efficient models for aqueous organic redox flow batteries

Jie Bao [a,*], Amanda Howard [a], Ayoub El Bendali [a,b], Yunxiang Chen [a], Yucheng Fu [a], Peiyuan Gao [a], Soowhan Kim [a], Tiffany Louie [a,c], Grace Yuan [a], Alvin Liu [a], Qixuan Jiang [a,d], Chao Zeng [a], Zhijie Xu [a], Panos Stinis [a,d], Wei Wang [a], Vincent Sprenkle [a]

[a] Pacific Northwest National Laboratory, Richland, WA, USA
[b] University Mohammed VI Polytechnic, Morocco
[c] Carnegie Mellon University, Pittsburgh, PA, USA
[d] University of Washington, Seattle, WA, USA

ARTICLE INFO

Keywords:
Aqueous organic redox flow battery
Commercial scale cell
Analytical model
Deep operator networks

ABSTRACT

The rising usage of intermittent energy has garnered the need for large scale energy storage systems. Redox flow batteries (RFB) based energy storage system shows promising potential. Numerical simulations and machine learning approaches have been widely used to study RFB performance. The development of autonomous material discovery framework and digital twin of energy storage system usually needs to query cell performance through fast response models. In this study, two computationally efficient models are introduced: a physics-based analytical flow battery model (EZBattery), and a machine learning operator model (Deep Operator Network, denoted by DeepONet). Both models can provide cell performance near instantly, and prediction accuracy was systematically examined on an application of evaluating the performances of a 780 cm^2 aqueous organic redox flow battery (AORFB), using potential anolyte candidates in dihydroxyphenazine (DHP)-based family of organic materials. A validated computationally expansive 3-dimensional multi-physics finite element model by COMSOL was used as the ground truth and provided the training data set for the DeepONet. 1280 samples were generated with 10 properties to mimic the different possible anolyte candidates, and the cell performances were evaluated under 10 different combined operating conditions. The accuracy comparisons for the two computationally efficient models show that both models can provide comparable accuracy in predicting cell charging/discharging voltage curves. DeepONet can provide slightly higher overall accuracy than EZBattery with faster calculation speed, but highly relies on the training dataset. EZBattery does not need a training dataset and can provide interpretable physics-based explanations of the results, while being more flexible to adjust to adapt any different cell designs, flow battery architectures, and electrolyte materials.

1. Introduction

Solar and wind power, also known as intermittent energy, have seen continuous growth in the last two decades as the world opted to develop renewable energy production. Wind and solar production have expanded to 14 % of U.S. electricity generation in 2023 [1]. However, the amount of power produced is dependent on time, season, and weather, making it inconsistent and often unable to keep up with supply and demand [2]. Thus, intermittent energy can be more effectively utilized through reliable energy storage. Intermittent energy resources, when strategically deployed, possess the potential to complement existing power generation infrastructure. Energy storage systems, such as batteries, can be used to accumulate energy during periods of low demand, which can then be released during peak demand periods. Energy storage systems in combination with renewable energy provide a responsive solution to fluctuations in demand [3].

Large scale energy storage systems have a rising significance in transitioning our economy to clean, carbon free energy. Such systems typically store energy for ten or more hours. Therefore, they can be used to balance supply and demand over long periods, contributing to a reliable and consistent supply of energy [4]. Among all the battery based techniques, flow batteries show great advantages of lower material and maintenance costs and higher safety over the traditional Li-ion based systems [5]. Aqueous Organic Redox Flow Batteries (AORFBs), using organic active materials in one or both sides of the cell, are a more cost-competitive solution, since the active organic species can be synthesized

* Corresponding author.
E-mail address: jie.bao@pnnl.gov (J. Bao).

https://doi.org/10.1016/j.est.2025.118134
Received 26 October 2024; Received in revised form 23 July 2025; Accepted 17 August 2025
Available online 19 August 2025

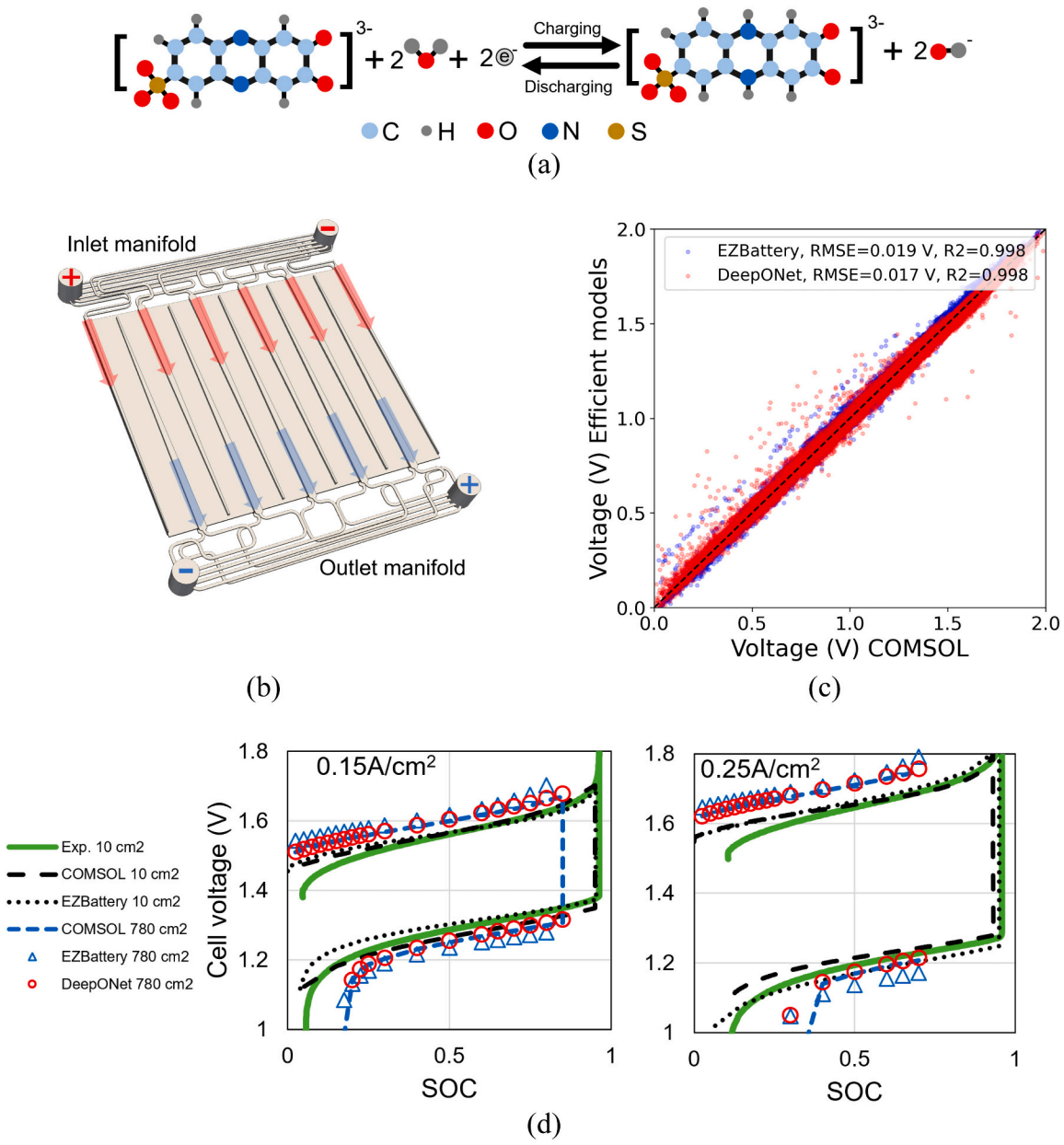

Fig. 1. Example sketch of the DHP-based family molecule structure and the electrochemical reaction (a); Geometry and the finite element simulation domain of the cell (b); A parity plot comparing two computationally efficient models (EZBattery and DeepONet) against the COMSOL FEM simulation results for all the test cases (c); Example of model validation for the cell charging/discharging performance for a 10 cm^2 cell with experimental measurements (60 mL/min flow rate), and the predictions for the upscaled 780 cm^2 cell (0.4 L/min flow rate) (d).

from low-cost and abundant materials [6,7].

Upscaling the new organic electrolyte materials' properties to the cell performance for different cell designs and operating conditions is crucial for material discovery and screening, system design and technical financial analysis, and developing a digital twin for the systems. A straightforward approach is numerically solving all the governing equations in the simulation domain of the specific cell geometry in 3-dimensional (3D) scheme. A lot of pioneering works [8–14] have demonstrated that this numerical approach is capable and accurate for various cells, from small lab-scale cell to large multi-cell stacks. However, such a numerical simulation approach on a 3D domain is computationally expensive, because all the governing equations are solved on the thousands to millions spatial discretized elements or meshes, such as in finite element (FEM) [15–17] and finite volume (FVM) [18,19] models, which may require a few hours to a few days to achieve converged solutions. Therefore, such an approach is not feasible or computationally efficient enough for the applications that need fast responses, such as the autonomous material discovery [20,21] framework and digital twins of energy storage systems [22,23], which usually query cell performance frequently with given material properties and/or operation conditions.

To accelerate the predictions from material properties to cell performance, zero-dimensional (0D) models are the most common method for cell performance prediction and optimization. 0D models simplify the cell into one point with assumptions of uniform concentration and overpotential in the cell [24–27]. With such simplifications, all the governing equations can be efficiently solved either numerically or by directly deriving analytical solutions. However, it is challenging for 0D models to resolve the species convection diffusion in the micro pores and channels of the electrode, so it usually is hard to accurately predict the performance of large cells when the less uniform concentrations of active species play a critical role.

For incorporating the non-uniform concentration of active species in the cell and the computational efficiency, a two-dimensional (2D) analytical model, EZBattery, has been developed and demonstrated for various cell applications in our previous work [28–30]. The EZBattery model simplifies the pore structure of the electrode into many micro-channels and derives an analytical solution of active species distribution in the micro-channel. This model can provide a computationally efficient prediction of the cell performance which is accurate when compared to the 3D FEM simulation solution.

In contrast to the physics-based models introduced above, machine learning based models are a powerful alternative to provide accurate prediction with high computational efficiency. A lot of pioneering works have introduced and demonstrated the application of machine learning model to flow battery performance prediction [24,31–33]. In this study, we introduce an application of operator learning with Deep Operator Networks (DeepONet) [34]. DeepONet have been successfully applied for modeling a wide variety of scientific problems [34–37]. They consist of two fully connected feed forward neural networks (FNNs), the branch network and the trunk network. When trained for AORFBs, the branch network takes as input the battery operating conditions and material properties, and the trunk network takes as input the state of charge (SOC). The branch and trunk network are trained simultaneously and combined with a dot product to predict the battery voltage at the given SOC.

In this work, the prediction accuracy of these two computationally efficient models, EZBattery and DeepONet, are systematically evaluated on a 780 cm^2 interdigitated cell for the possible anolyte candidates in dihydroxyphenazine (DHP)-based organic materials family. There are 1280 anolyte candidate materials and 10 different combined cell operation conditions, so there are in total 12,800 cases. The commercial FEM package COMSOL Multiphysics® was used to solve all the cases with a 3D scheme to serve as the ground truth. The 3D FEM solutions were used to train the DeepONet model and to evaluate the accuracy of both the DeepONet and EZBattery models. The details about the generation of 12,800 cases, the COMSOL FEM simulations, the EZBattery analytical solutions, and the DeepONet model construction and training are introduced in Section 2. The results of the accuracy comparisons for the two models show that both models can provide comparable accuracy of the prediction of cell charging/discharging voltage curves, with significantly reduced computational time cost compared with full 3D simulations. The DeepONet model provides overall slightly higher accuracy than EZBattery with faster calculation speed once trained, however, the disadvantage of operator learning models is the need to generate a training dataset and train the model. EZBattery does not need a training dataset and can provide physics explanations of the results, and is more flexible, so it can be adjusted to adapt to any cell design, flow battery architecture, and electrolyte material. Detailed results and discussions are in Section 3.

2. Methodology

In this study, the performance of potential anolyte candidates from the dihydroxyphenazine (DHP)-based family of organic materials are used to evaluate the model prediction accuracy. The catholyte is kept as ferro/ferricyanide. The electrochemical reaction for anolyte is genderized as:

$$\left[DHP-G_f\right]^{n-}+2H_2O+2e^- \underset{Discharge}{\overset{Charge}{\rightleftarrows}} \left[DHP-G_f-2H\right]^{n-}+2OH^-, \quad (1)$$

where G_f stands for the functional groups, and n stands for the charge. One example of the organic molecule structure (7,8-dihydroxyphenazine-2-sulfonic acid) and the electrochemical reaction in alkaline solution are sketched in Fig. 1(a).

The high-fidelity 3D multi-physics FEM is considered as a reference, so the fast-forward analytical model EZBattery and a machine-learning based DeepONet model are evaluated against the solutions from the 3D FEM. The property ranges of the anolyte candidates are listed in Table 1. Those property ranges are determined according to previous experiment database and/or model estimations [7,38–58]. Please note that the mass transfer coefficient in Table 1 is a dimensionless number. The relationship between the mass transfer coefficient and the dimensional mass transfer rate (with unit m/s) is discussed in Section 2.2. The Latin Hypercube sampling (LHS) method was used to randomly sample the properties in the range to generate 1280 samples for the 10 properties to mimic the different possible anolyte candidates. The cell operates at five different pump flow rates (0.4, 0.8, 1.2, 1.6, 2.0 L/min) and two current densities (1600, 2400 A/m^2). All 1280 samples are tested under those operation conditions which yields a total of 12,800 cases. The three models (3D FEM, fast-forward analytical model EZBattery, and machine learning model DeepONet) are used to evaluate the performance of these anolyte candidates. The explanations for these three models are in Sections 2.1 to 2.3.

Table 1
The properties' range for the possible anolyte candidates.

Property's name	Unit	Min	Max	Mean
Charge transfer coefficient	1	0.3	0.7	0.5
Electrode specific area	1/m	1.2×10^{4}	1.2×10^{5}	6.5×10^{4}
Membrane conductivity	S/m	0.5	2.0	1.25
Reaction rate constant	m/s	1.0×10^{-8}	1.5×10^{-3}	5.9×10^{-4}
Mass transfer coefficient	1	0.5	50	25.25
Initial concentration	mol/m^3	50	1500	775
Species diffusivity	m^2/s	4.9×10^{-11}	4.9×10^{-9}	2.4×10^{-9}
Electrolyte viscosity	Pa•s	1.0×10^{-3}	1.2×10^{-2}	6.5×10^{-3}
Standard potential	V	−1.4	−0.1	−0.75
Anolyte conductivity	S/m	10	100	55

2.1. 3D finite element model

For evaluating the potential candidate organic anolyte material in a commercial scale flow battery stack, the 3-dimensional multi-physics numerical simulation is a straightforward approach. In this study, a 780 cm^2 interdigitated cell is used as a representative design for evaluating the potential candidate anolyte. The cell geometry is shown in Fig. 1(b). This cell design, characterized by dimensions of 30 cm in width and 26 cm in length, incorporates six inlet flow channels and five outlet channels (the two inlet channels at the edges of the cell are only have half width of other channels). The electrode, with a thickness of 0.64 mm, is complemented by a membrane with a thickness of 508 μm. The red arrows in Fig. 1(b) mark the inlet channels, and the blue arrows mark the outlet channels. The inlet and outlet manifold, as marked in in Fig. 1(b), are for equalizing the length of the flow path to the main flow pipes for all the channels. The positive signs on the two main flow pipes are for transportation of positive side electrolyte, and the negative signs on the two main flow pipes are for transportation of negative side electrolyte.

The multi-physics model includes the fluid mass and momentum conservation equations, electrolyte chemical species convection and diffusion equations, and charge conservation equations [9]. The charge conservation equations combine with the Ohm's law as:

$$-\sigma_s^{eff}\nabla^2\phi_s = S_\phi, \quad (2)$$

$$-\kappa_l^{eff}\nabla^2\phi_l = S_\phi, \quad (3)$$

where ϕ_s and ϕ_l are the electronic potential field in solid electrode and ionic potential in liquid electrolyte, respectively. σ_s^{eff} is the effective electronic conductivity in solid electrode, and κ_l^{eff} is the effective ionic conductivity in liquid electrolyte. S_ϕ is the source term that can be expressed as $\pm aj_i$. a is the specific area of the electrode, j is the local current density, and the positive sign is for solid electrode (Eq. (2)), and

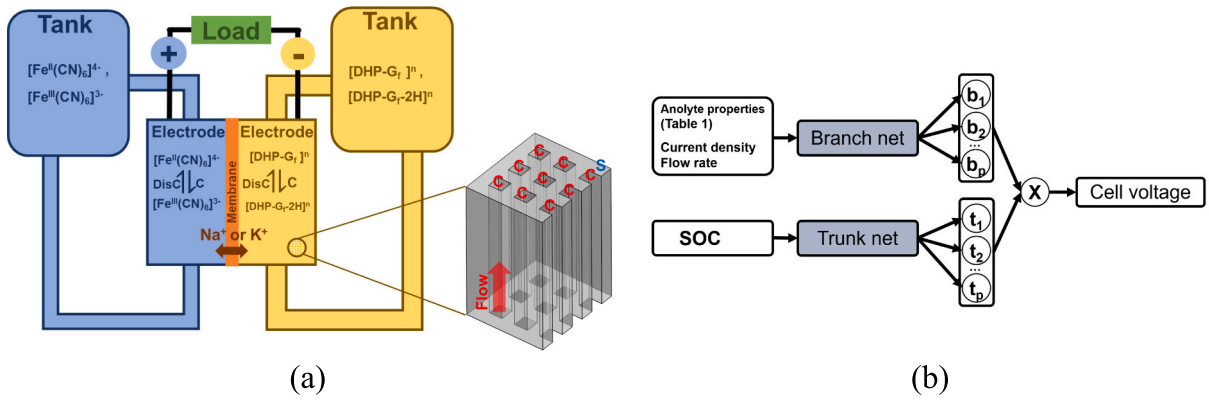

Fig. 2. Sketch of the EZBattery model configuration for AORFB and the simplified micro channels for electrodes (a); Sketch of the DeepONet structure (b).

negative sign is for liquid electrolyte (Eq. (3)). The subscript $i = 1$ represents the positive side and $i = 2$ represents the negative side of the cell. The local current density can be evaluated by Butler-Volmer's law:

$$j_i = Fk_i\sqrt{C_O^s C_R^s}\left[exp\left(\frac{\beta z F\eta_i}{RT}\right) - exp\left(-\frac{(1-\beta)zF\eta_i}{RT}\right)\right], \tag{4}$$

where F is the Faraday constant, k is the reaction rate constant, C is the species concentration, β is the charge transfer coefficient, z is the number of electrons involved in the reaction, R is universal gas constant, T is temperature, and η is the activation overpotential. The subscript O stands for the oxidized state species, and the subscript R stands for the reduced state species. The superscript s represents the concentration on the electrode solid surface. The activation overpotential also satisfies the relation [25,59]:

$$\eta_i = \phi_s - \phi_l - E_i^{OCV}, \tag{5}$$

where E^{OCV} is the equilibrium potential or open circuit voltage (OCV) estimated by Nernst equations [25,59]:

$$E_i^{OCV} = E_i^0 + \frac{RT}{zF}ln\left(\frac{C_O}{C_R}\right), \tag{6}$$

where E^0 is the standard potential for the positive or negative side redox couples. The charge conservation Eqs. (2) and (3) are coupled together through Eqs. (4) to (6). With solved charge source term S_ϕ, the source term for species convection diffusion equations can be estimated by S_ϕ/zF. The solution to the species convection diffusion equations provides the information on the species concentration, which are used in Eqs. (4) and (6). In this study, it is assumed that the species transport and reaction do not affect the liquid flow transport, so the fluid mass and momentum conservation equations only provide the flow field information to the species convection diffusion equations. The species concentration on electrode wall C^s usually depends on the bulk concentration C, averaged pore diameter, diffusion coefficient, and rate of reaction. A commonly used estimation was provided by H. Al-Fetlawi et al. [59]. For example, the reduced state species concentration on the pore wall surface can be estimated by

$$C_R^s = \frac{C_R + \epsilon k e^{-F\left(\phi_s-\phi_l-E^0\right)/(2RT)}\left(\frac{C_R}{\gamma_O} + \frac{C_O}{\gamma_R}\right)}{1 + \epsilon k\left(\frac{e^{-\frac{F\left(\phi_s-\phi_l-E^0\right)}{(2RT)}}}{\Upsilon_O} + \frac{e^{\frac{F\left(\phi_s-\phi_l-E^0\right)}{(2RT)}}}{\Upsilon_R}\right)}, \tag{7}$$

where Υ_O and Υ_R are the oxidized and reduced state species piston velocity respectively. It is defined as the ratio between the diffusivity and averaged pore size [59]. ϵ is the porosity.

All the equations are solved by COMSOL Multiphysics® in the simulation domain shown in Fig. 1(b), and the model has been validated against experiment data in our previous work [13,14]. As introduced above, there are 1280 anolyte candidates and 10 different combined cell operation conditions, so there are in total 12,800 simulation cases, and each case costs about one hour on 128 CPU cores. These 12,800 cases results are used as the ground truth to evaluate the fast-forward analytic model EZBattery, and divided to be used as the training, validation, testing datasets for the DeepONet machine learning model. An example of comparisons of the three models' predictions and the experiment measurements are shown in Fig. 1(d). The experimental measured charging/discharging curves for a 10 cm^2 cell are shown in green. The corresponding model predictions for this 10 cm^2 cell are shown in black dash line and dot line for COMSOL and EZBattery models respectively. This 10 cm^2 cell was tested with 0.15 A/cm^2 and 0.25 A/cm^2 with 60 mL/min flow rate. More details for this 10 cm^2 cell experiment are provided in C. Zeng et al. [13]. The charging/discharging curves for the 780 cm^2 cell are estimated by the three models in blue dash line, blue triangles, and red circles for COMSOL, EZBattery, and DeepONet respectively. This large cell performance is evaluated at 0.15 A/cm^2 and 0.25 A/cm^2 with 0.4 L/min flow rate.

2.2. Fast-forward analytical model: EZBattery

As introduced in the finite element model, it is computationally expensive to solve all the coupled governing equations. Therefore, the EZBattery model provides analytical solutions by simplifying all the pores in the electrode into micro-channels. The sketch of the EZBattery model configuration for the AORFB and the simplified micro-channels for the electrode are shown in Fig. 2(a). The letters "C" mark the channels, and "S" marks the solid electrode (Fig. 2(a)). The transport of reaction species in porous electrode, using the reduced state species concentration (C_R) as the example, can be modeled by the convection diffusion equation

$$\frac{\partial C_R}{\partial t} + \vec{U} \bullet \nabla C_R = D_R \nabla^2 C_R, \tag{8}$$

where $\vec{U}$ is flow velocity, and D_R is effective diffusivity of this reduced state species. In the simplified micro-channel, the size of the channel is controlled by the pore size and porosity of the electrode. The convection diffusion equation can be represented in cylindrical coordinate system as

$$\frac{\partial C_R}{\partial t} + u(r)\frac{\partial C_R}{\partial x} = D_r\left(\frac{\partial^2 C_R}{\partial x^2} + \frac{d}{r}\frac{\partial C_R}{\partial r} + \frac{\partial^2 C_R}{\partial r^2}\right), \tag{9}$$

where x is spatial coordinate along channel flow direction, r is spatial

coordinate along channel radius direction, d is channel shape parameter (0 and 1 denote square and circular). The solution to Eq. (9) can be expressed as the Taylor series expansion around the center line of the channel as

$$C_R(x,r,t) = C_R^c + \sum_{i=1}^{+\infty} \frac{r^{2i}}{(2i)!} C_R^{c,2i}, \tag{10}$$

where C_R^c is the concentration along the centerline of the channel, and $C_R^{c,2i}$ denotes even order derivatives with respect to r. Applying the reduced boundary method [60], dropping the terms with order higher than 5, and considering steady state, Eq. (9) can be simplified for the concentration along the centerline as

$$\frac{d+3}{2} u_0 \frac{\partial C_R^c}{\partial x} - D_R \frac{\partial^2 C_R^c}{\partial x^2} = -\frac{3(d+1) i_s}{Fb}, \tag{11}$$

where i_s is an averaged local current density on micro-channel wall surface [30], b is pore size or micro-channel size, u_0 is the averaged flow velocity. More detailed steps from Eqs. (9) to (11) are discussed in Supporting Information Section S1 and Y. Chen et al. [30]. Eq. (11) is a second order linear homogeneous equation with constant coefficients, which has a general solution [61]. By applying the general solution on Eq. (11) and normalizing the concentration, the species concentration along the center line can be estimated by:

$$\begin{aligned} \widehat{C}_R^c = SOC &- \frac{6(d+1)}{d+3} \frac{I_{cu}}{\beta_m} \left(\frac{x}{b} - \gamma Pe \right) \\ &- \frac{12(d+1)}{(d+3)^2} \frac{I_{cu}}{Pe\beta_m} \left[e^{\frac{d+3}{2} Pe \left(\gamma Pe - \frac{H}{b} \right)} - e^{\frac{d+3}{2} Pe \frac{x-H}{b}} \right], \end{aligned} \tag{12}$$

where $\widehat{C}_R^c$ is the dimensionless concentration of reduced state species along the center line of the micro-channel. The dimensionless concentration is normalized by the initial total concentration of the reduced and oxidized state species. H is flow cell height, I_{cu} is relative importance of current density to advection [30], γ is concentration entrance length constant (0.033), SOC is the state of charge, and Pe is the Peclet number. β_m is mass transfer coefficient. It is a factor that correct the differences of mass transfer rate between channel and real electrode pore structure. The relationship between the mass transfer coefficient (β_m) and the mass transfer rate (k_m) is defined as $k_m = \beta_m k_m^T$, where k_m^T is theoretical mass transfer rate in channel. k_m^T can be estimated as $k_m^T = \frac{u_0}{\left(\frac{5}{16} - 2\gamma\right) Pe + \frac{2H}{b} - \frac{4}{3Pe}}$.

Both mass transfer rate (k_m) and theoretical mass transfer rate (k_m^T) are dimensional number with unit m/s. The mass transfer coefficient (β_m) is a dimensionless number, which is ranging between 0.5 and 50 in this study as listed in Table 1. Substituting the solution of $\widehat{C}_R^c$ (Eq. (12)) into Eq. (10), the species concentration along wall surface of the micro-channel can be estimated by

$$\begin{aligned} \widehat{C}_R^s = SOC &- \left[\frac{5}{16} - \frac{6(d+1)}{d+3} \gamma \right] \frac{I_{cd}}{\beta_m} - \frac{6(d+1)}{d+3} \frac{I_{cu}}{b\beta_m} x \\ &- \frac{12(d+1)}{(d+3)^2} \frac{I_{cu}}{Pe\beta_m} \left[e^{\frac{d+3}{2} Pe \left(\gamma Pe - \frac{H}{b} \right)} - e^{\frac{d+3}{2} Pe \frac{x-H}{b}} \right], \end{aligned} \tag{13}$$

where $\widehat{C}_R^s$ is the dimensionless concentration of reduced state species on the wall surface of the micro-channel, and I_{cd} is relative importance of current density to diffusion [30].

The accuracy of this proposed simplification, using micro-channels to represent porous structure, has been quantitatively evaluated by C. Zeng et al. [62] with experimental measurements. The experiments used a 10 cm^2 cell to measurement the mass transfer rate by testing the cell at different flow rates, ranging from 2 mL/min to 80 mL/min (average flow velocity from 1 mm/s to 4 cm/s). The estimated mass transfer rate, as determined by the simplified micro-channel theory, closely matches the experiment measurements when the average flow velocity lower than 1.5 cm/s, which is shown in reference [62] Figs. 4 and 6. This velocity is equivalent to approximately 2.3 L/min flow rate for the 780 cm^2 cell, which is sufficiently high for practical operations.

With these analytical solutions for the concentrations, the activation overpotential is estimated by:

$$\eta = \frac{RT}{\beta F} ln \left(\frac{I_{ck}}{2\sqrt{\widehat{C}_R^s (1 - \widehat{C}_R^s)}} + \sqrt{\frac{I_{ck}^2}{4\widehat{C}_R^s (1 - \widehat{C}_R^s)} + 1} \right), \tag{14}$$

where I_{ck} is relative importance of current density to reaction. The equilibrium potential can be calculated through Eq. (6) by using the analytical solution of concentration along the center line of the micro-channel $\widehat{C}_R^c$. The total cell voltage is estimated by $E_{cell} = E^{OCV} + \eta + E_{ohm}$, where E_{ohm} is Ohmic voltage loss in the cell. More detailed explanations for the terms in the analytical solutions and the mathematical derivations are available in Chen et al. [28–30]. This analytical model has been named as EZBattery for short, and released at GitHub (github.com/pnnl/EZBattery). An important note is that the EZBattery model does not need to be calibrated to match the results from the 3D FEM simulations. Both models (EZBattery and COMSOL) share the same values for all the cell parameters and material properties.

This study focused on the (DHP)-based family of organic electrolyte redox flow battery, but EZBattery model is capable of handling various electrolytes, such as vanadium redox flow battery [28–30], zinc-iodine flow battery [63], and Prussian blue/white redox targeting flow battery [64]. The example model setups for the zinc-iodine flow battery and Prussian blue/white redox targeting flow battery are available in the EZBattery GitHub repository (github.com/pnnl/EZBattery).

For modeling different types of flow batteries, the model requires the values of the main material properties, the number of electrons involved in the electrochemical reaction, whether water is involved in the reaction, stoichiometric numbers of the reaction, etc. For flow batteries with two charge/discharge plateaus, such as another widely studied bipyridinium-based cell [65], in addition to applying the corresponding material properties for the bipyridiniums-based electrolyte, modeling needs to account for the separation of the current density between the two electrochemical reactions or the two steps of the electrochemical reaction. The detailed introduction and equations are provided in Supporting Information Section S2.

2.3. Deep operator network model

Deep operator networks (DeepONets) are neural operators that learn the mapping between two Banach spaces [34]. Standard DeepONets consist of two neural networks, named the branch and the trunk. The branch takes as input the dependent variables, in this case the operating conditions and material properties of the battery. The trunk takes as input the independent variables, in this case the SOC. The outputs of the branch and trunk networks are combined with a dot product to give a prediction of the battery voltage as a function of the SOC, electrolyte properties, and the battery operating conditions. The sketch of the DeepONet structure for estimating the cell performance is shown in Fig. 2(b). Because the same value of the SOC can be used for charging and discharging, we append a 1 to the branch input to indicate charging and − 1 to indicate discharging. In this work we use modified DeepONet [66], which introduce two encoder layers for the branch and trunk. The encoder layers are combined with the branch and trunk network in a convex combination at each hidden layer. This change has been shown to increase the expressivity of the network and reduce the model error [66]. The DeepONet is implemented in JAX [67]. For this work we use branch and trunk networks that each have 4 hidden layers with 200 neurons each and the hyperbolic tangent activation function. The

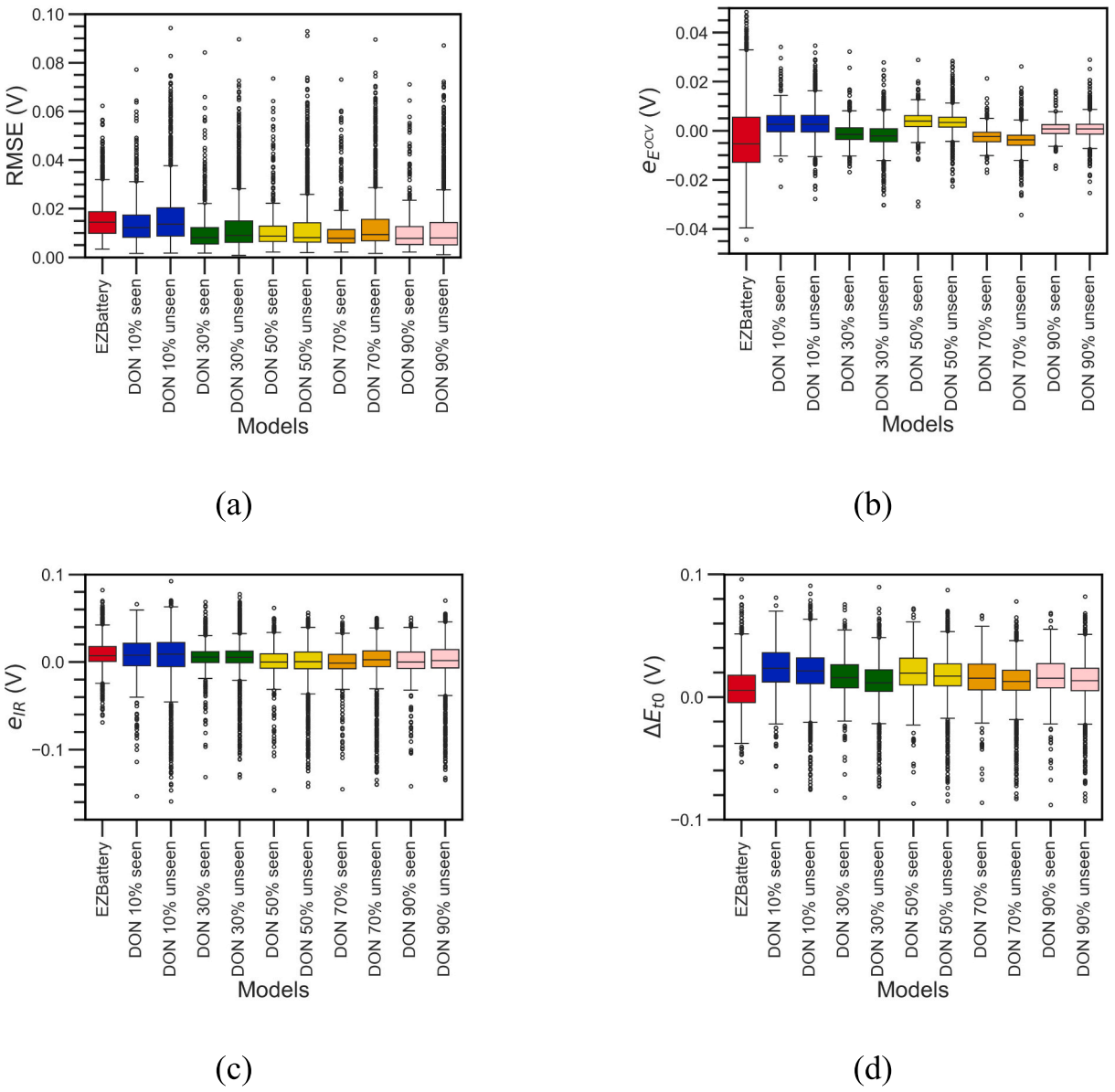

Fig. 3. Model accuracy evaluation metrics on the 2630 test cases for EZBattery and DeepONet (noted as DON for short in the figure labels) trained by 10 % to 90 % dataset. (a) RMSE, (b) $e_{E^{OCV}}$, (c) e_{IR}, (d) ΔE_{t0}.

learning rate follows an exponential decay scheduler with initial value 1^{-4}, 2000 decay steps, and a decay rate of 0.99. We train for 600,000 iterations with a batch size of 300 (operating condition, SOC) pairs.

An important consideration when doing machine learning is the size of the training set. In order to train an accurate model, the training set must comprehensively cover the range of expected operating conditions. This is because neural operators struggle with extrapolation beyond the conditions seen in training. The data used for training the DeepONet is generated by COMSOL 3D simulations of AORFBs. In this study, not all the 1280 candidate anolyte can operate physically at the 10 different operating conditions. By removing the non-operational cases, the full dataset has 9990 cases. They are divided into 10 batches by the 10 operating conditions. Each batch has fixed flow rate and current density. To generate the training set, we first exclude two full batches to use in the test set (current density = 1600 A/m^2 and flow rate = 1.2 L/min; current density = 2400 A/m^2 and flow rate = 1.6 L/min). From the remaining eight batches we randomly select 10 % to use as the test set. For the eight batches data (the eight operating conditions), we chose between 10 % and 90 % to be the training set. This allows us to study the amount of data needed for training the DeepONet model, which ultimately allows for minimizing the cost of data generation. The total size of the test set is 2630 simulation cases. The training set ranges from 816 simulations for 10 % of the data to 7360 for 90 % of the data.

3. Results

3.1. Metrics for evaluating different models

Because of the high computational cost of the COMSOL FEM simulation, the cell performance is modeled at 19 SOCs each for both charging and discharging conditions, so totally 38 SOCs for each case. To balance the computational cost and accurately capture the rapid increase or decrease stages of the charging/discharging curve, a finer resolution of SOC was used during the potentially rapid changing stages, while a coarser resolution was employed during the slower changing stages. The modeled SOCs range from 0.025 to 0.85, at 0.025 increments when the SOC is between 0.025 and 0.25, 0.1 increments when SOC is between 0.3 and 0.6, and 0.05 increments when the SOC is between 0.6

and 0.85. The comparison between the model predictions for the test set is shown in Fig. 1(c). The vertical axis is for the two computationally efficient models. The red dots represent DeepONet, and blue dots represent EZBattery. The horizontal axis is for the FEM simulation results by COMSOL. In general, both models' predictions concentrate around the 'identity line' (dash line in Fig. 1(c)). The overall root mean square errors (RMSE) for all the data points in Fig. 1 (c) are 0.019 and 0.017 V for EZBattery and DeepONet respectively. The R^2 are 0.998 for both EZBattery and DeepONet, as noted in Fig. 1(c).

To quantify the differences between the predictions from EZBattery or DeepONet model and the COMSOL FEM simulation results, four metrics are defined: the charging/discharging curve RMSE, error $e_{E^{OCV}}$, error e_{IR}, and ΔE_{t0}. The charging/discharging curve RMSE for the cell performance prediction is defined as:

$$RMSE = \sqrt{\frac{1}{N}\left[\sum_{SOC}\left(V^{c'}{}_{SOC} - V^{c}_{soc}\right)^2 + \sum_{SOC}\left(V^{dc'}{}_{SOC} - V^{dc}_{soc}\right)^2\right]}, \tag{15}$$

where $V^{c'}{}_{SOC}$ is the cell charging voltage at given SOC predicted by either EZBattery or the DeepONet, and V^{c}_{soc} is the cell charging voltage at a given SOC predicted by the COMSOL FEM simulation. Similarly, $V^{dc'}{}_{SOC}$ is the cell discharging voltage predicted by either EZBattery or the DeepONet, and V^{dc}_{soc} is the cell discharging voltage predicted by the COMSOL FEM simulation. N is the total number of SOCs that is compared between the models. Please note that N is not always 38, because a lot of anolyte candidates and/or cell operating conditions cannot make the cell charge to SOC = 0.85 or discharge to SOC = 0.025.

Since the RMSE is always positive, it cannot justify whether EZBattery or the DeepONet over or underestimates the cell voltage compared with the COMSOL FEM simulations. Errors e_E and e_{IR} can provide such information, and are expressed as:

$$e_{E^{OCV}} = \frac{1}{N}\left[\sum_{SOC}\left(V^{c'}{}_{SOC} - V^{c}_{soc}\right) + \sum_{SOC}\left(V^{dc'}{}_{SOC} - V^{dc}_{soc}\right)\right], \tag{16}$$

$$e_{IR} = \frac{1}{N_c}\sum_{SOC}\left(V^{c'}{}_{SOC} - V^{c}_{soc}\right) - \frac{1}{N_{dc}}\sum_{SOC}\left(V^{dc'}{}_{SOC} - V^{dc}_{soc}\right), \tag{17}$$

where N_c is the number of SOCs for charging, and N_{dc} is the number of SOCs for discharging. For comparing the charging/discharging voltage curves, $e_{E^{OCV}}$ evaluates the errors more contributed from the OCV E^{OCV}, while e_{IR} focuses more on evaluating the errors contributed from the internal resistances. In the scenario that the OCV is predicted accurately, the errors caused by the internal resistances would lead to the opposite signs of errors for changing and discharging voltage, which makes $e_{E^{OCV}}$ is near zero but e_{IR} counts all the errors. In contrast, for the scenario that the OCV is deviate from the true value, but the internal resistances are accurately estimated, e_{IR} would be nearly zero but $e_{E^{OCV}}$ counts all the errors. The fourth metric ΔE_{t0} is the voltage difference at the start of charging between the EZBattery or the DeepONet prediction and the COMSOL FEM simulation.

As introduced in Section 2.3, the DeepONet model was trained using a training set generated from COMSOL FEM simulation results. The training set used 10 % to 90 % anolyte candidate properties in 8 out of 10 operation conditions as the training dataset. It used all the anolyte candidates in 2 out of 10 operation conditions and 10 % anolyte candidate properties in the rest of the 8 operation conditions as the testing dataset. In total, we used 2630 cases in the testing dataset for evaluating the DeepONet prediction accuracy against COMSOL FEM simulation results. For the 8 operation conditions that were partially used the training dataset, the corresponding testing dataset is named as "seen", which includes 667 cases. The 2 operation conditions that were not used in the training dataset is named as "unseen", which includes 1963 cases. The EZBattery model does not need any results from COMSOL FEM simulation results to calibrate the model, so it can provide predictions for all the 12,800 cases. However, for fairly comparing the EZBattery and DeepONet models, the same 2630 cases mentioned above were used to evaluate the four metrics for both models. The distribution of the RMSE, $e_{E^{OCV}}$, e_{IR} and ΔE_{t0} derived from both EZBattery and DeepONet model predictions for the 2630 cases are plotted in boxplot shown in Fig. 3 (a) to (d) respectively. The "seen" and "unseen" operation conditions testing dataset are plotted separately in Fig. 3 for evaluating the capability of interpolating sparse information.

For the RMSE (Fig. 3 (a)), the mean of the RMSEs for all the 2630 test cases for the EZBattery model is 0.015 V, and the largest RMSE for the EZBattery model is 0.065 V. For the DeepONet model, when using 10 % data to train, the RMSEs are slightly larger than the performance of the EZBattery RMSE generally. After using 30 % or more data to train the DeepONet, the mean of the RMSEs for all the 2630 test cases reduces to around 0.01 V. Using more than 30 % data to train the model does not significantly improve the model prediction accuracy, indicating that 30 % of the training data is sufficient. Although the DeepONet model using 30 % or more data to train provide lower mean and quantiles of RMSE distributions, there are some extreme cases where the RMSE values can near 0.1 V (the outliers points in Fig. 3 (a)), which is slightly worse than the performance of EZBattery model.

The results from the distribution of $e_{E^{OCV}}$ (Fig. 3 (b)) show that EZBattery performs worse than all DeepONet models that are trained with 10 % to 90 % of the training data. The most extreme $e_{E^{OCV}}$ for EZBattery are 0.048 V and -0.044 V. Based on the definition of error $e_{E^{OCV}}$ (Eq. (16)), the EZBattery model possibly has higher error on estimation

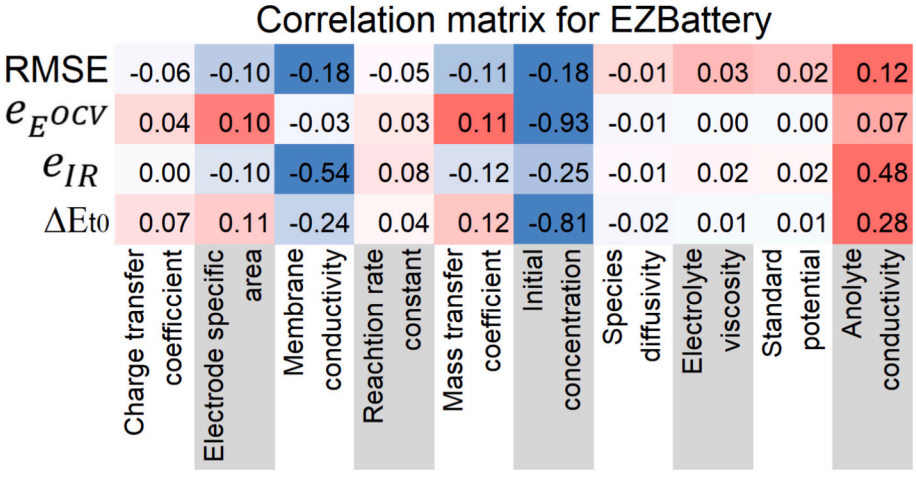

Fig. 4. The correlation matrix of the model accuracy evaluation metrics for EZBattery model.

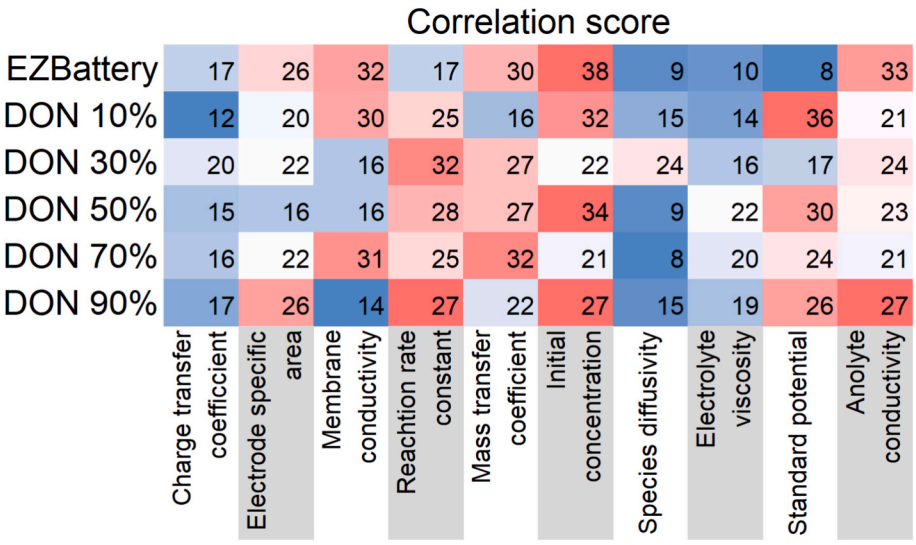

Fig. 5. Correlation score matrix for all the EZBattery and DeepONet models (noted as DON for short in the labels).

of OCV. In comparison, the DeepONet models have the most extreme cases for $e_{E^{OCV}}$ within ±0.035 V, and the 0.25 to 0.75 quantile is within ±0.005 V. This indicates that the trained DeepONet models can highly possibly capture the equilibrium potential accurately. Additionally, increasing the training dataset from 10 % to 90 % of the total data, can slightly improve the error $e_{E^{OCV}}$. Please note that although the EZBattery model predictions show higher errors $e_{E^{OCV}}$ than the DeepONet predictions, controlling the errors in ±0.05 V is still considerably accurate.

The results from the distribution of error e_{IR} (Fig. 3 (c)) show that the predictions for the EZBattery model outperforms the DeepONet models. Based on the definition of e_{IR} (Eq. (17)), it focuses more on errors of the estimation on cell internal resistances. Therefore, the EZBattery model provides better accuracy on cell internal resistance calculations. The 0.25 to 0.75 quantile are in the range between 0 and 0.01 V, and the worst situations are also controlled within ±0.1 V. In comparison, the DeepONet models show larger errors for the 0.25 to 0.75 quantile, and the worst situations can make error higher than 0.15 V. Additionally, after 30 % of the data for training, using more data does not improve the model accuracy.

For ΔE_{t0}, EZBattery is slightly better than all the DeepONet models. The 0.25 to 0.75 quantile of ΔE_{t0} for EZBattery is closer to 0, and the extreme simulations are controlled between −0.05 to 0.1 V. In comparison, the worst situation for DeepONet models usually reach −0.1 V.

For the "unseen" operation condition testing dataset, the DeepONet models can provide the similar accuracy as the "seen" operation condition testing dataset for all the four metrics. This indicates that the proposed DeepONet model shows sufficient accuracy on interpolating of the sparse data in training dataset.

3.2. Correlation between the evaluation metrics and the properties of the anolyte candidates

The correlation matrix is the most adapted tool to quantitatively assess the relationships between the model parameters and model outputs, highlighting both strong and weak correlations that may influence the model prediction errors. The correlation matrix of the model accuracy evaluation metrics for the EZBattery model is shown in Fig. 4. The values are calculated by the Pearson method [68] between these parameters: RMSE value, $e_{E^{OCV}}$, e_{IR}, ΔE_{t0}, and the 10 properties of anolyte candidates: charge transfer coefficient, specific area, membrane conductivity, reaction rate constant, mass transfer coefficient, initial concentration, diffusivity, electrolyte viscosity, standard potential, and electrolyte conductivity. The values are between ±1. A value far away from zero means the quantity is important, and a value near zero means the quantity is less important. The correlation matrix can help to understand the sources of errors. For example, the correlation value for initial concentration is −0.93 for the $e_{E^{OCV}}$. This provides two indications. First, the property "initial concentration" contributes more to determination of the cell performance, and second, the algorithms that use "initial concentration" to calculate the cell performance are not accurate enough, leading to relatively higher $e_{E^{OCV}}$. The "initial concentration" is mainly involved in the calculation of equilibrium potential, which is consistent with the $e_{E^{OCV}}$ distribution for EZBattery (Fig. 3 (b)), where the EZBattery model possibly has higher error estimating the equilibrium potential, as discussed in Section 3.1. As mentioned in Section 3.1, the e_{IR} focus more on cell internal resistances, and the correlation values "membrane conductivity" and "electrolyte conductivity" show higher values, which are −0.54 and 0.48 respectively. This is also consistent with the common understanding of the physics-based model that the internal resistances mainly rely on these two material ionic conductivities. Similarly, both RMSE and ΔE_{t0} are the overall estimation on the errors, so the higher correlation values are on anolyte initial concentration, membrane conductivity, and electrolyte conductivity.

For summarizing the overall correlation between all the accuracy evaluation metrics (RMSE, $e_{E^{OCV}}$, e_{IR}, and ΔE_{t0}) and the anolyte properties for EZBattery model, a score system is designed. Points are assigned based on these conditions: the highest value receives 10 points, and the lowest receives 1 point. If two or more values are identical, they receive the same number of points. The correlation scores for EZBattery model are shown in Fig. 5 the first row. The same correlation matrix evaluations were applied to the DeepONet model (10 % to 90 % dataset for training), and summarized by the same score system as shown in Fig. 5 in the 2nd row to the 6th row.

Because EZBattery is a physics-based model, the correlation is more physically explainable. The initial concentration is related to the estimation of equilibrium potential, the membrane and electrolyte conductivities are related to the calculation of Ohmic resistance, the specific area and mass transfer coefficient are related to the calculation of activation potential. From the scores in Fig. 5, the EZBattery model firstly needs to improve the algorithm for the equilibrium potential that can minimize the difference between simplified micro-channel geometry and the realistic interdigitated large cell designs. For further improvements, EZBattery models can also improve the algorithm for the Ohmic resistance calculations. For the DeepONet models, since it is completely data driven model, it is hard to provide the physical explanations and

Table 2
Comparisons of the two models: EZBattery and DeepONet.

	EZBattery	DeepONet
Features	• Physics-based model. • Analytical solution. • Computational efficient.	• Machine learning model. • Achieve high accuracy with small amount of training data. • Computational efficient for inference.
Pros	• Less than 0.1 s to provide one charging-discharging cycle. • The results are explainable. • Does not need training dataset. • Can be directly used to predict the cell with various cell setup/configuration.	• Less than 0.01 s to provide one charging-discharging cycle. The trained model costs less than EZBattery to predict cell performance. • Higher accuracy than EZBattery, if sufficient training dataset is provided.
Cons	• The model prediction accuracy may be limited by the assumptions and/or simplifications in the model. • Needs to provide the values for all the parameters/properties in the model. • For higher accuracy, the model still needs case by case calibration with the experiment data.	• Need the training dataset. • Only can predict the cell performance within the setup/configurations in the training dataset. • The result is not explainable.

the potential model improvement insights from the sources of the errors in Fig. 5. However, it shows that with more data used in the training, the errors sources are more evenly distributed among the 10 properties of the anolyte candidates. This phenomenon indicates that the machine learning model has potential trends to discover and utilize the minor relationships in the coupled physic-based governing equations for improving the model prediction accuracy.

4. Conclusions and discussions

Two computationally efficient models, EZBattery and DeepONet, are introduced and demonstrated for evaluating the commercial scale cell performance for potential anolyte candidates in dihydroxyphenazine (DHP)-based family of organic materials. The accuracy of the two models is evaluated against the 3D multi-physics FEM in the commercial package COMSOL. This 3D multi-physics FEM has been validated with experimental measurements for vanadium redox flow batteries [14] and organic dihydroxyphenazine sulfonate (DHPS) anolyte flow batteries [13]. The models are evaluated on examples of 1280 anolyte candidate materials at 10 different operating conditions. Both models provide considerably accurate prediction of the cell performance with significantly reduced computational costs. The EZBattery model costs less than 0.1 s to provide one charging-discharging cycle predictions, and the trained DeepONet only costs 0.01 s to provide the similar predictions, while the 3D FEM simulation requires around 1 h on 128 CPU cores. A summary of the comparisons between the two models are listed in Table 2. The trained DeepONet model can provide the prediction faster than EZBattery. Although the time cost looks negligible, for the system level digital twin, cell diagnosis framework, and autonomous material discovery framework, the model needs to provide thousands to millions of predictions for different operating conditions and SOCs frequently. Therefore, such time cost differences can still lead to huge computational efficiency advantage. The DeepONet, as a machine learning model, needs a training dataset, so it is not as flexible as EZBattery to adapt to any adjustments on flow battery cell designs. In future work we will consider the situation where there is no or insufficient training data. In this case, EZBattery can be used to generate data for the DeepONet training for fully utilizing the flexibility of EZBattery and the inference computation efficiency of DeepONet.

Additionally, EZBattery can be used to evaluate the importances of the material properties on cell performance metrics. An example is shown in Fig. 6. EZBattery model estimated the performance metrics of a

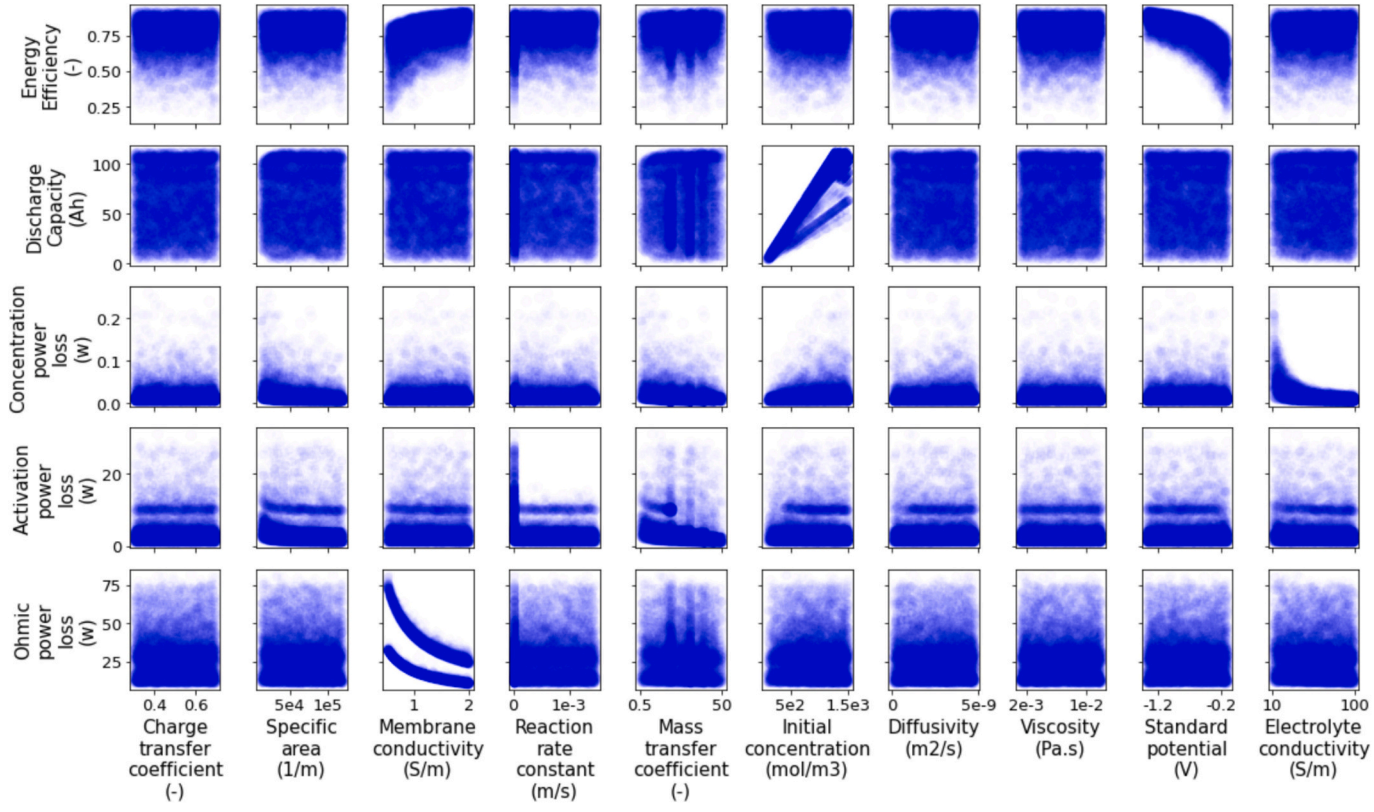

Fig. 6. Correlation between the material properties and the 780 cm^2 cell performance metrics.

780 cm^2 cell, such as energy efficiency, discharge capacity, concentration power loss, activation power loss, and Ohmic power loss through approximately 10,000 cases. It is evident that higher membrane conductivity and more negative standard potential for anolyte lead to higher energy efficiency. The higher initial concentration, representing solubility, results in higher discharge capacity. The Ohmic power loss is primarily controlled by membrane conductivity. The two curves shown in the subfigure for membrane conductivity versus Ohmic power loss are due to the evaluation of cell performance at only two current densities (1600, 2400 A/m^2). Due to the extremely high computational efficiency of EZBattery model, this example sensitivity analysis required only around 1 CPU hour to collect all the necessary data. However, using the COMSOL FEM model to collect a similar amount data for such sensitivity analysis costed over 1 million CPU hours [69] on high-performance computing (HPC) cluster, resulting in significant expense and energy consumption.

CRediT authorship contribution statement

Jie Bao: Writing – review & editing, Writing – original draft, Visualization, Validation, Supervision, Software, Resources, Methodology, Investigation, Data curation, Conceptualization. **Amanda Howard:** Writing – review & editing, Writing – original draft, Software, Methodology, Data curation, Conceptualization. **Ayoub El Bendali:** Writing – original draft, Visualization, Validation, Methodology, Data curation, Conceptualization. **Yunxiang Chen:** Validation, Software, Methodology, Data curation, Conceptualization. **Yucheng Fu:** Writing – review & editing, Methodology, Data curation, Conceptualization. **Peiyuan Gao:** Visualization, Validation, Software, Methodology, Data curation, Conceptualization. **Soowhan Kim:** Writing – review & editing, Data curation. **Tiffany Louie:** Writing – original draft, Visualization, Validation, Data curation. **Grace Yuan:** Writing – original draft, Visualization, Data curation. **Alvin Liu:** Writing – original draft, Validation, Data curation. **Qixuan Jiang:** Validation, Software, Methodology, Data curation, Conceptualization. **Chao Zeng:** Visualization, Validation, Software, Methodology, Data curation, Conceptualization. **Zhijie Xu:** Validation, Supervision, Resources, Methodology, Conceptualization. **Panos Stinis:** Supervision, Methodology, Conceptualization. **Wei Wang:** Supervision, Resources, Project administration, Funding acquisition, Conceptualization. **Vincent Sprenkle:** Supervision, Resources, Project administration, Funding acquisition, Conceptualization.

Funding information

Energy Storage Materials Initiative (ESMI), a Laboratory Directed Research and Development Project at Pacific Northwest National Laboratory (PNNL).

U.S. Department of Energy (DOE) Office of Electricity's Rapid Operational Validation Initiative (ROVI).

Declaration of competing interest

The authors declare that they have no known competing financial interests or personal relationships that could have appeared to influence the work reported in this paper.

Acknowledgments

This research was supported by Energy Storage Materials Initiative (ESMI), which is a Laboratory Directed Research and Development Project at Pacific Northwest National Laboratory (PNNL), and U.S. Department of Energy (DOE) Office of Electricity's Rapid Operational Validation Initiative (ROVI). PNNL is a multiprogram national laboratory operated for the U.S. Department of Energy (DOE) by Battelle Memorial Institute under Contract no. DEAC05–76RL01830.

Appendix A. Supplementary data

Supplementary data to this article can be found online at https://doi.org/10.1016/j.est.2025.118134.

Data availability

Data will be made available on request.

References

[1] What is U.S. electricity generation by energy source?, Available from: https://www.eia.gov/tools/faqs/faq.php?id=427&t=3, 2024.
[2] Intermittent Generation, Available from: https://energytransition.nema.org/intermittent-generation/, 2024.
[3] Intermittent Renewable Energy, Energy & Services, Available from: https://www.bpa.gov/energy-and-services/efficiency/demand-response/intermittent-renewable-energy, 2024.
[4] Long Duration Storage Shot, Available from: https://www.energy.gov/eere/long-duration-storage-shot, 2021.
[5] X. Liu, et al., Low-cost all-iron flow battery with high performance towards long-duration energy storage, J. Energy Chem. 73 (2022) 445–451.
[6] R. Feng, et al., Reversible ketone hydrogenation and dehydrogenation for aqueous organic redox flow batteries, Science 372 (6544) (2021) 836–840.
[7] A. Hollas, et al., A biomimetic high-capacity phenazine-based anolyte for aqueous organic redox flow batteries, Nat. Energy 3 (2018) 508–514.
[8] E. Knudsen, et al., Flow simulation and analysis of high-power flow batteries, J. Power Sources 299 (2015) 617–628.
[9] C. Yin, et al., A coupled three dimensional model of vanadium redox flow battery for flow field designs, Energy 74 (2014) 886–895.
[10] Q. Zheng, et al., A three-dimensional model for thermal analysis in a vanadium flow battery, Appl. Energy 113 (2014) 1675–1685.
[11] S. Kim, et al., 1 kW/1 kWh advanced vanadium redox flow battery utilizing mixed acid electrolytes, J. Power Sources 237 (2013).
[12] Y. Fu, et al., A three-dimensional pore-scale model for redox flow battery electrode design analysis, J. Power Sources 556 (2023) 232329.
[13] C. Zeng, et al., Characterization of electrochemical behavior for aqueous organic redox flow batteries, J. Electrochem. Soc. 169 (12) (2022).
[14] C. Zeng, et al., In situ characterization of kinetics, mass transfer, and active electrode surface area for vanadium redox flow batterie, J. Electrochem. Soc. 170 (2023) 030507.
[15] A. Hrennikoff, Solution of problems of elasticity by the framework method, J. Appl. Mech. 8 (4) (1941) 169–175.
[16] R. Courant, Variational methods for the solution of problems of equilibrium and vibrations, Bull. Am. Math. Soc. 49 (1943) 1–23.
[17] COMSOL, Simulate real-world designs, devices, and processes with multiphysics software from COMSOL, Available from: https://www.comsol.com/, 2024.
[18] S.V. Patankar, Numerical Heat Transfer and Fluid Flow, 1st ed., CRC Press, 1980.
[19] Simcenter, Simcenter STAR-CCM+ CFD software, Available from: https://plm.sw.siemens.com/en-US/simcenter/fluids-thermal-simulation/star-ccm/, 2024.
[20] N.J. Szymanski, et al., An autonomous laboratory for the accelerated synthesis of novel materials, Nature 624 (2023) 86–91.
[21] A.G. Kusne, et al., On-the-fly closed-loop materials discovery via Bayesian active learning, Nat. Commun. 11 (2020) 5966.
[22] ESMI. Energy Storage Materials Initiative (ESMI), Available from: https://www.pnnl.gov/projects/energy-storage-materials-initiative-esmi, 2024.
[23] ROVI. Rapid Operational Validation Initiative (ROVI), Available from: https://www.energy.gov/oe/rapid-operational-validation-initiative-rovi, 2024.
[24] Q. He, et al., Enhanced physics-constrained deep neurtal networks for modeling vanadium redox flow battery, J. Power Sources 542 (2022).
[25] A.A. Shah, et al., A dynamic unit cell model for the all-vanadium flow battery, J. Electrochem. Soc. 158 (6) (2011) A671–A677.
[26] D.E. Eapen, S.R. Choudhury, R. Rengaswamy, Low grade heat recovery for power generation through electrochemical route: Vanadium Redox Flow Battery, a case study, Appl. Surf. Sci. 474 (2019) 262–268.
[27] A.K. Sharma, et al., Verified reduction of dimensionality for an all-vanadium redox flow battery model, J. Power Sources 279 (2015) 345–350.
[28] Y. Chen, et al., A two-dimensional analytical unit cell model for redox flow battery evaluation and optimization, J. Power Sources 506 (2021) 230192.
[29] Y. Chen, et al., A hybrid analytical and numerical model for cross-over and performancev decay in a unit cell vanadium redox flow battery, J. Power Sources 578 (2023) 233210.
[30] Y. Chen, et al., Analytical modeling for redox flow battery design, J. Power Sources 482 (2021) 228817.
[31] Y. Fu, et al., Physics-guided continual learning for predicting emerging aqueous organic redox flow battery material performance, ACS Energ. Lett. 9 (2024) 2767–2774.
[32] W. Chen, Y. Fu, P. Stinis, Physics-informed machine learning of redox flow battery based on a two-dimensional unit cell model, J. Power Sources 584 (2023) 233548.
[33] Q. He, P. Stinis, A.M. Tartakovsky, Physics-constrained deep neural network method for estimating parameters in a redox flow battery, J. Power Sources 528 (2022).

[34] L. Lu, et al., Learning nonlinear operators via DeepONet based on the universal approximation theorem of operators, Nat. Mach. Intell. 3 (2021) 218–229.
[35] S. Mao, et al., PPDONet: deep operator networks for fast prediction of steady-state solutions in disk–planet systems, Astrophys. J. Lett. 950 (2023).
[36] A.A. Howard, et al., Multifidelity deep operator networks for data-driven and physics-informed problems, J. Comput. Phys. 493 (2023) 112462.
[37] L. Xu, H. Zhang, M. Zhang, Training a deep operator network as a surrogate solver for two-dimensional parabolic-equation models, J. Acoust. Soc. Am. 154 (2023) 3276–3284.
[38] K. Amini, et al., An extremely stable, highly soluble monosubstituted anthraquinone for aqueous redox flow batteries, Adv. Funct. Mater. 33 (13) (2023) 2211338.
[39] J. Cao, et al., A highly reversible anthraquinone-based anolyte for alkaline aqueous redox flow batteries, J. Power Sources 386 (2018) 40–46.
[40] C. de la Cruz, et al., A systematic study on the redox potentials of phenazine-derivatives in aqueous media: a combined computational and experimental work, ChemSusChem 16 (8) (2023) e202201984.
[41] S. Guiheneuf, et al., A new hydroxyanthraquinone derivative with a low and reversible capacity fading process as negolyte in alkaline aqueous redox flow batteries, J. Power Sources 539 (2022) 231600.
[42] J.D. Hofmann, et al., Quest for organic active materials for redox flow batteries: 2,3-Diaza-anthraquinones and their electrochemical properties, Chem. Mater. 30 (3) (2018) 762–774.
[43] Y. Ji, et al., A phosphonate-functionalized quinone redox flow battery at near-neutral pH with record capacity retention rate, Adv. Energy Mater. 9 (12) (2019) 1900039.
[44] S. Jin, et al., A water-miscible quinone flow battery with high volumetric capacity and energy density, ACS Energ. Lett. 4 (6) (2019) 1342–1348.
[45] Y. Jing, et al., Anthraquinone flow battery reactants with nonhydrolyzable water-solubilizing chains introduced via a generic cross-coupling method, ACS Energy Lett. 7 (1) (2022) 226–235.
[46] E.F. Kerr, et al., High energy density aqueous flow battery utilizing extremely stable, branching-induced high-solubility anthraquinone near neutral pH, ACS Energ. Lett. 8 (1) (2023) 600–607.
[47] D.G. Kwabi, et al., Alkaline quinone flow battery with long lifetime at pH 12, Joule 2 (9) (2018) 1894–1906.
[48] S. Pang, et al., Biomimetic amino acid functionalized phenazine flow batteries with long lifetime at near-neutral pH, Angew. Chem. Int. Ed. 60 (10) (2021) 5289–5298.
[49] P. Sun, et al., 110th anniversary: unleashing the full potential of quinones for high performance aqueous organic flow battery, Ind. Eng. Chem. Res. 58 (10) (2019) 3994–3999.
[50] C. Wang, et al., High-performance alkaline organic redox flow batteries based on 2-Hydroxy-3-carboxy-1,4-naphthoquinone, ACS Energ. Lett. 3 (10) (2018) 2404–2409.
[51] C. Wang, et al., Alkaline soluble 1,3,5,7-tetrahydroxyanthraquinone with high reversibility as anolyte for aqueous redox flow battery, J. Power Sources 524 (2022) 231001.
[52] C. Wang, et al., N-alkyl-carboxylate-functionalized anthraquinone for long-cycling aqueous redox flow batteries, Energy Storage Mater. 36 (2021) 417–426.
[53] K. Wedege, Draevi, Organic redox species in aqueous flow batteries: redox potentials, chemical stability and solubility, Sci. Rep. 6 (1) (2016) 39101.
[54] N.P.N. Wellala, et al., Decomposition pathways and mitigation strategies for highly-stable hydroxyphenazine flow battery anolytes, J. Mater. Chem. A 9 (38) (2021) 21918–21928.
[55] M. Wu, et al., Highly stable, low redox potential quinone for aqueous flow batteries**, Batt. Superc. 5 (6) (2022) e202200009.
[56] X. Xia, et al., A high-capacity 1, 2:3, 4-dibenzophenazine anode integrated into carbon felt for an aqueous organic flow battery in alkaline media, Green Chem. 24 (22) (2022) 8783–8790.
[57] J. Xu, et al., Ultrastable aqueous phenazine flow batteries with high capacity operated at elevated temperatures, Joule 5 (9) (2021) 2437–2449.
[58] P. Gao, et al., Graphical Gaussian process regression model for aqueous solvation free energy prediction of organic molecules in redox flow batteries, Phys. Chem. Chem. Phys. 23 (43) (2021) 24892–24904.
[59] H. Al-Fetlawi, A.A. Shah, F.C. Walsh, Non-isothermal modelling of the all-vanadium redox flow battery, Electrochim. Acta 55 (1) (2009) 78–89.
[60] Z. Xu, A reduced-boundary-function method for convective heat transfer with axial heat conduction and viscous dissipation, J. Heat Mass Transf. 134 (7) (2012) 071705.
[61] M. Braun, Differential Equations and Their Applications: An Introduction to Applied Mathematics, 4th ed., Springer, 1992.
[62] C. Zeng, et al., In situ characterization of kinetics, mass transfer, and active electrode surface area for vanadium redox flow batteries, J. Electrochem. Soc. 170 (3) (2023) 030507.
[63] B. Li, et al., Ambipolar zinc-polyiodide electrolyte for a high-energy density aqueous redox flow battery, Nat. Commun. (2015) 6.
[64] S. Yan, et al., Redox targeting-based neutral aqueous flow battery with high energy density and low cost, Chem. Sustain. Energ. Mater. 16 (19) (2023) e202300710.
[65] Q. Chen, et al., Organic electrolytes for pH-neutral aqueous organic redox flow batteries, Adv. Funct. Mater. 32 (9) (2021) 2108777.
[66] S. Wang, H. Wang, P. Perdikaris, Improved architectures and training algorithms for deep operator networks, J. Sci. Comput. 92 (2022).
[67] J. Bradbury, et al., JAX: Composable Transformations of Python+NumPy Programs, Available from: http://github.com/jax-ml/jax, 2018.
[68] F. Galton, Regression towards mediocrity in hereditary stature, J. Anthropol. Inst. G. B. Irel. 15 (1886) 246–263.
[69] Y. Chen, et al., A hybrid numerical and machine learning framework for evaluating the performance of a 780 cm aqueous organic redox flow battery, J. Power Sources 635 (2025) 236470.